

Communication

Construction of Core–Shell CoMoO₄@ γ -FeOOH Nanosheets for Efficient Oxygen Evolution Reaction

Huijun Song^{1,†}, Jingjing Li^{1,†}, Guan Sheng^{2,†}, Yinling Zhang¹, Ahmad Azmin Mohamad² , Juan Luo¹, Zhangnan Zhong¹ and Wei Shao^{1,*}

¹ State Key Laboratory Breeding Base of Green Chemistry Synthesis Technology, College of Chemical Engineering, Zhejiang University of Technology, Hangzhou 310014, China; huijunsong@126.com (H.S.); 18855492938@163.com (J.L.); 2111901117@zjut.edu.cn (Y.Z.); luojuang2021@163.com (J.L.); zhongzhangnan@126.com (Z.Z.)

² School of Materials and Mineral Resources Engineering, Universiti Sains Malaysia, Nibong Tebal 14300, Penang, Malaysia; shengguan@student.usm.my (G.S.); aam@usm.my (A.A.M.)

* Correspondence: weishao@zjut.edu.cn

† These authors contributed equally to this work.

Abstract: The oxygen evolution reaction (OER) occurs at the anode in numerous electrochemical reactions and plays an important role due to the nature of proton-coupled electron transfer. However, the high voltage requirement and low stability of the OER dramatically limits the total energy converting efficiency. Recently, electrocatalysts based on multi-metal oxyhydroxides have been reported as excellent substitutes for commercial noble metal catalysts due to their outstanding OER activities. However, normal synthesis routes lead to either the encapsulation of excessively active sites or aggregation during the electrolysis. To this end, we design a novel core–shell structure integrating CoMoO₄ as support frameworks covered with two-dimensional γ -FeOOH nanosheets on the surface. By involving CoMoO₄, the electrochemically active surface area is significantly enhanced. Additionally, Co atoms immerse into the γ -FeOOH nanosheet, tuning its electronic structure and providing additional active sites. More importantly, the catalysts exhibit excellent OER catalytic performance, reducing overpotentials to merely 243.1 mV a versus 10 mA cm⁻². The current strategy contributes to advancing the frontiers of new types of OER electrocatalysts by applying a proper support as a multi-functional platform.

Keywords: γ -FeOOH nanosheets; CoMoO₄@ γ -FeOOH heterojunction; oxygen evolution reaction



Citation: Song, H.; Li, J.; Sheng, G.; Zhang, Y.; Mohamad, A.A.; Luo, J.; Zhong, Z.; Shao, W. Construction of Core–Shell CoMoO₄@ γ -FeOOH Nanosheets for Efficient Oxygen Evolution Reaction. *Nanomaterials* **2022**, *12*, 2215. <https://doi.org/10.3390/nano12132215>

Academic Editors: Francesc Viñes Solana and Stefano Agnoli

Received: 2 June 2022

Accepted: 27 June 2022

Published: 28 June 2022

Publisher's Note: MDPI stays neutral with regard to jurisdictional claims in published maps and institutional affiliations.



Copyright: © 2022 by the authors. Licensee MDPI, Basel, Switzerland. This article is an open access article distributed under the terms and conditions of the Creative Commons Attribution (CC BY) license (<https://creativecommons.org/licenses/by/4.0/>).

1. Introduction

Developing renewable energy technologies is of great significance for lowering the growing rate of energy consumption and mitigating the deterioration of the living environment [1–6]. However, the sustainable energy sources, primarily solar and wind, have so far impeded the large-scale practical application of renewable energy. To solve this issue, electrocatalytic water splitting, consisting of an oxygen evolution reaction (OER) and a hydrogen evolution reaction (HER), is a promising approach to generating sustainable H₂ from water without using additional reactants. However, the sluggish kinetics of the OER at the anode involves a complex four-step proton-coupled electron transfer process and is regarded as a thermodynamic- and kinetic rate-limiting reaction. Therefore, it is essential to explore efficient electrocatalysts that can effectively facilitate an OER. Even though Ir-/Ru-based oxides show outstanding electrocatalytic behaviors for OER, the high cost and scarcity of these noble catalysts significantly impedes their large-scale applications. To this end, the development of efficient OER catalysts that are inexpensive, easily accessible, and demonstrate excellent electrocatalytic performance (exhibiting a lower overpotential, a high Faradaic efficiency, and adequate catalytic stability) as substitutes for noble metal-based catalysts is both highly important and urgent.

Newly developed OER catalysts can be classified into two types. Metal-free nanomaterials such as carbon nanotube (CNT), graphene, and boron nitride are reported as efficient OER electrocatalysts; however, these catalysts always require multi-step functionalization and are sensitive to pH in the system [7,8]. On the other hand, first-row transition metal (Mn, Fe, Co, Ni, etc.) based OER catalysts (such as layered double hydroxides (LDHs) [9,10], metal oxides [11], phosphides [12], selenides [13], sulfides [14], and nitrides [15]) have attracted enormous attention as next-generation OER catalysts due to their abundance. These transition metal catalysts have proven to exhibit outstanding OER performances; however, recent works suggest that most of these OER catalysts will undergo structural self-reconstruction during the electrolysis process [16]. More specifically, oxyhydroxides are inevitably formed through the electro-oxidation of these pre-catalysts, which are identified as the real active sites for OER. Nevertheless, most self-reconstructions of pre-catalysts generally occur exclusively on the surface of pre-catalysts, leading to the formation of the typical core-shell (pre-catalysts@oxyhydroxides) structures, in which large amounts of inactive reaction sites are buried in the core [17]. In addition, a sophisticated process and additional amounts of energy consumption are usually required for the re-construction of pre-catalysts. Thus, exploring the direct wet-chemical synthesis of oxyhydroxides with fantastic performance for OERs is of great importance. The layered γ -type iron oxyhydroxide (γ -FeOOH) has been reported to exhibit superior OER performance; however, its layered crystal structure and sheet-shaped morphology tend to make γ -FeOOH nanosheets aggregate because of the high surface energy, which severely diminishes the number of exposed active sites [18]. An effective strategy to overcome this drawback involves constructing heterostructures in which the arrayed γ -FeOOH nanostructures are decorated on other nanomaterials as a substrate with a robust structural stability. Moreover, the desired interfaces between the nanostructures could regulate the electron configuration of the active site as well as the activity owing to the coupling interfaces and the synergistic effect of the heterostructures. For example, the trimetallic phosphate (Fe-Co-Ni-P-1) has been reported to exhibit faster kinetics and a better long-term stability in the catalytic process, which is mainly attributed to monodisperse core-shell structure-induced low resistance, the large electrochemically active area, and the synergistic effect among metals [19]. Wang's group has recently reported that the core-shell structure of Au@NiCo₂S₄ core-shell NPs could result in a higher proportion of high-valence Ni/Co cations and improve its electronic conductivity, which collectively enhances its OER catalytic performance [20]. In addition, a great number of the heterostructures have also been fabricated for an improved electrocatalytic performance, such as CoP/FeP₄ [21], Co₉S₈/CoO/NC [22], CoFeS₂@CoS₂ [23], Ni-P-S@FeOOH/CC [24], Ni₅P₄/Ni₂P-FeNi [25], and MnO-OVs/NCNTs [26].

Considering the above discussion, we develop herein a facial strategy to construct core-shell CoMoO₄@ γ -FeOOH nanosheets grown on nickel foam by the interface engineering strategy. The obtained CoMoO₄@ γ -FeOOH core-shell nanosheet structures are composed of arrayed γ -FeOOH nanosheets anchored on CoMoO₄ nanosheets. The synergistic effect provides the CoMoO₄@ γ -FeOOH core-shell nanosheets with a highly electrochemically active surface area due to the core CoMoO₄'s support as well as highly and intrinsically active sites with a Co atom-modified γ -FeOOH shell layer. The designed CoMoO₄@ γ -FeOOH nanosheets exhibit a remarkable OER catalytic performance, requiring overpotentials of only 243.1 and 278.5 mV to obtain 10 and 100 mA cm⁻², respectively, with a negligible degradation after 36 h of OER electrolysis at multi current densities.

2. Materials and Methods

2.1. Reagents and Chemicals

Cobalt nitrate hexahydrate (Co(NO₃)₂·6H₂O), sodium molybdate dihydrate (Na₂MoO₄·2H₂O), potassium ferrate (K₂FeO₄), sodium hydroxide NaOH, and acetone were analysis reagents (AR) and purchased from Aladdin Biochemical Technology Co. Ltd. (Shanghai, China). Ethanol and hydrogen chloride (HCl) were of AR grade and obtained

from Shanghai Macklin Biochemical Technology Co., Ltd. (Shanghai, China). Ruthenium oxide (RuO₂) was provided by Sigma-Aldrich (St. Louis, MO, USA).

2.2. Methods

For the synthesis of Ni foam supported CoMoO₄, 0.175 g Co(NO₃)₂·6H₂O (0.6 mmol) and 0.145 g Na₂MoO₄·2H₂O (0.6 mmol) were dissolved in 5 mL deionized water (DI water) under sonication. These two transparent solutions were mixed under continuous stirring for 0.5 h and then transferred into a 25 mL Teflon-lined autoclave. A piece of Ni foam (1.0 × 3.0 cm²) was thoroughly rinsed with 1.0 M HCl, acetone, and ethanol in sequence under sonication in a 20 mL glass vial. The pretreated Ni foam was put into the autoclave mentioned above, and then the mixed system was kept at 150 °C for 4 h. The Ni foam samples were taken out, washed, and vacuum dried, and CoMoO₄ arrays were obtained.

For the synthesis of Ni foam supported CoMoO₄@γ-FeOOH, 7.5 mM K₂FeO₄ solution containing 6 M NaOH was firstly prepared by dissolving K₂FeO₄ into aqueous NaOH solution under sonication and then centrifuged at 9000 rpm for 1 min. Subsequently, the as-prepared CoMoO₄ was soaked into 20 mL of the above solution. After reacting for 24 h at ambient conditions without any disruption, the obtained CoMoO₄@γ-FeOOH was cleaned with deionized water and then dried naturally. The Ni foam supported γ-FeOOH was also synthesized via a similar procedure, except for the fact that the CoMoO₄ was replaced with pretreated Ni foam.

2.3. Materials Characterizations

Scanning electron microscope (SEM) images were collected with a field-emission scanning electron microscope ZEISS-G500 (ZEISS, Jena, Germany) at an accelerating voltage of 5 kV. The as-synthesized samples were scraped from the Ni foam and analyzed with a Titan Themis Z (Thermo Fisher Scientific, Waltham, MA, USA) to record high-resolution TEM (HRTEM) images, elemental mapping, and SAED patterns. The Raman spectra of all synthesized samples were obtained using a HORIBA Jobin–Yvon Lab-Ram ARAMIS (Horiba, Kyoto, Japan) Raman spectrometer equipped with a CCD detector. X-ray diffraction, D8Advance (Bruker, Billerica, MA, USA) was used for the crystalline phase analysis with Cu Kα radiation. The surface properties of all samples were characterized using X-ray photoelectron spectroscopy (XPS) ESCALAB 250, (Thermo Fisher Scientific, Waltham, MA, USA). All binding energies were calibrated with the C 1 s peak at 284.8 eV corresponding to adventitious carbon found on the surface.

2.4. Electrochemical Measurements

All the electrochemical tests were conducted in fresh 1.0 M KOH on a CHI 760E electrochemical station using a standard three-electrode system. The as-prepared catalysts that were grown on the Ni foam (0.5 × 1.0 cm²) directly served as the working electrode. The standard Hg/HgO electrode was applied as the reference electrode, while a platinum wire was used as the counter electrode. All the measured potentials were calibrated to a reversible hydrogen electrode (RHE): RHEs: $E_{\text{RHE}} = E_{\text{Hg}/\text{HgO}} + 0.059 \times \text{pH} + 0.098$ (V). Linear sweep voltammetry (LSV) with 95% iR compensation was carried out at a scan rate of 0.5 mV s⁻¹. Multicurrent densities were applied for measuring long-term electrochemical stability. The double-layer capacitance (C_{dl}) was estimated based on the cyclic voltammograms (CVs) recorded at various scan rates over a non-faradaic potential range of 1.024–1.124 V (E_{RHE}).

3. Results and Discussion

Figure 1 illustrates the procedure for constructing Ni foam-supported hierarchical 2D core–shell CoMoO₄@γ-FeOOH nanosheets. In brief, the CoMoO₄ nanosheets were uniformly grown on Ni foam through a reported hydrothermal method with some modifications, followed by an immersion treatment with a mixed solution containing K₂FeO₄ and NaOH at room temperature for 24 h to prepare the core–shell structured CoMoO₄@γ-FeOOH nanosheets. This core–shell structure could effectively prevent the high surface

energy of γ -FeOOH nanosheet-induced aggregation, which could increase the number of exposed active sites and the electrochemically active surface area (ECSA) of γ -FeOOH nanosheets. Scanning electron microscopy (SEM) images showed the morphological and structural evolution process of the as-prepared catalysts. As shown in Figure 2a–c, the as-prepared CoMoO_4 presents micrometer-length nanosheets similar to the reported results [27]. In addition, the as-prepared CoMoO_4 nanosheets on the Ni foam surface displayed a uniform coverage, and the thickness of a single nanosheet was about ~ 30 nm. After reacting in the solution containing K_2FeO_4 and NaOH , the SEM images (Figure 2d–f) show that the surface of the CoMoO_4 nanosheets turned rough and was decorated with some worm-like γ -FeOOH nanomaterials. In addition, the thickness of the CoMoO_4 increased to 120 nm. A high-angle annular dark-field scanning transmission electron microscopy (HAADF-STEM) image (Figure 2g) shows that these worm-like γ -FeOOH nanomaterials are actually tiny nanosheets. The corresponding energy-dispersive X-ray spectroscopy (EDS) mapping images of a vertical $\text{CoMoO}_4@ \gamma$ -FeOOH nanosheet clearly show that the Mo and Fe elements are mainly distributed in the core and shell of the $\text{CoMoO}_4@ \gamma$ -FeOOH nanosheets, respectively, while the Co and O elements are homogeneously distributed over the entire hierarchical 2D core–shell $\text{CoMoO}_4@ \gamma$ -FeOOH nanosheets. To further elucidate the element distribution of the shell (tiny γ -FeOOH nanosheets) of the $\text{CoMoO}_4@ \gamma$ -FeOOH hierarchical nanosheets, the EDS mapping of horizontal $\text{CoMoO}_4@ \gamma$ -FeOOH hierarchical nanosheets and a line scan were performed. As shown in Figure S1, Fe has the largest dispersion area and exhibits more content than Co on the edge of the tiny γ -FeOOH, and there is almost no Mo signal on the tiny γ -FeOOH nanosheet. However, the content of Co is higher than Fe in the interior of the tiny γ -FeOOH, suggesting the probable ion exchange of Co and Fe during the formation of γ -FeOOH. Such ion exchange reactions could promote the nucleation of γ -FeOOH on the surface of CoMoO_4 and benefit the formation of a core–shell structure of $\text{CoMoO}_4@ \gamma$ -FeOOH. The pure γ -FeOOH nanosheets supported on the Ni foam were also prepared as the monophasic counterpart. The SEM images (Figure S2a–c) show that the tiny γ -FeOOH nanosheets were vertically and uniformly grown on the Ni foam, exhibiting a similar morphology to the shell of the $\text{CoMoO}_4@ \gamma$ -FeOOH hierarchical nanosheets. Nevertheless, the pure γ -FeOOH powder synthesized without the Ni foam substrate exhibited a highly stacked morphology (Figure S2d).

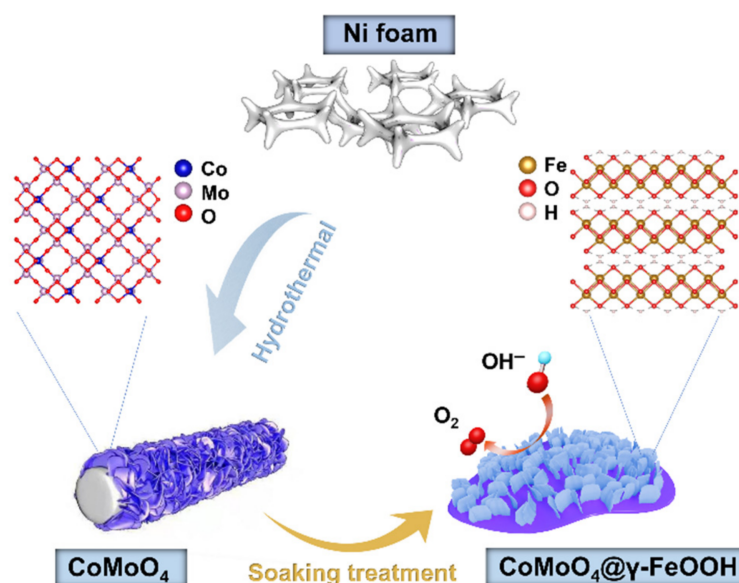


Figure 1. Schematic illustration for the construction of $\text{CoMoO}_4@ \gamma$ -FeOOH OER catalyst.

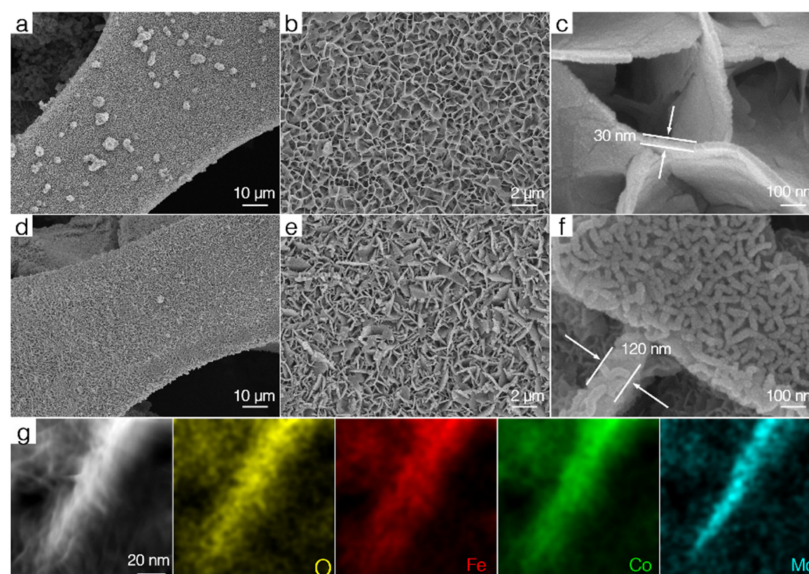


Figure 2. SEM images of (a–c) CoMoO_4 and (d–f) $\text{CoMoO}_4@ \gamma\text{-FeOOH}$. (g) HAADF-STEM and the corresponding EDS mapping images of $\text{CoMoO}_4@ \gamma\text{-FeOOH}$.

A powder X-ray diffraction (PXRD) was carried out to investigate the structural information. As shown in Figure S3a, the main diffraction peaks of the CoMoO_4 nanosheets could be assigned to CoMoO_4 (PDF no. 25-1434). Following the reaction in the mixed solution containing K_2FeO_4 and NaOH , no apparent new diffraction peaks were observed in the $\text{CoMoO}_4@ \text{Fe}$ based nanosheets compared with that of CoMoO_4 , suggesting that $\gamma\text{-FeOOH}$ possessed a lower crystallinity and that the core retained the structure of CoMoO_4 . The pure $\gamma\text{-FeOOH}$ was also characterized (Figure S3b) and several weak diffraction peaks that adequately matched the $\gamma\text{-FeOOH}$ could be found [28]. To further confirm the formation of $\text{CoMoO}_4@ \gamma\text{-FeOOH}$, Raman tests were conducted. As shown in Figure S4, the bands located at 326, 846, and 935 cm^{-1} for the Co–O–Mo, O–Mo–O, and Mo–O vibrations, respectively, could be found in both the CoMoO_4 and $\text{CoMoO}_4@ \gamma\text{-FeOOH}$ nanosheets [29], while the Raman band located at 230, which could likely be ascribed to Fe–O vibrations, could be found in both the $\gamma\text{-FeOOH}$ and $\text{CoMoO}_4@ \gamma\text{-FeOOH}$ nanosheets [18]. This spectra information indicates the co-existence of CoMoO_4 and $\gamma\text{-FeOOH}$ in the $\text{CoMoO}_4@ \gamma\text{-FeOOH}$ nanosheets. The HRTEM imaging allowed for the atomic-scale structural identification of $\text{CoMoO}_4@ \gamma\text{-FeOOH}$ nanosheets. Figure 3a shows the low magnification TEM image of the $\text{CoMoO}_4@ \gamma\text{-FeOOH}$ nanosheets, from which we can tell that its morphology comprises a bunch of intersecting layers. The yellow rectangular area in the inset is the CoMoO_4 component and the red one represents the $\gamma\text{-FeOOH}$ nanosheets growing upon the much larger CoMoO_4 sheets as the matrix. The HRTEM image (Figure 3b) and its corresponding diffractogram (Figure 3d) after the implementation of the Fast Fourier Transform (FFT) of the $\gamma\text{-FeOOH}$ nanosheets reveal the $\{200\}$ planes where the lattice spacing is 1.5 Å and the $\{002\}$ planes where the lattice spacing is 3.5 Å; the nanosheets' identification was confirmed from crystallography since it adequately matches the crystalline model of $\gamma\text{-FeOOH}$ observed along the $[010]$ axis (Figure 3c) and the corresponding simulated FFT pattern (Figure 3e). Similar to what was mentioned previously, the HRTEM image and corresponding Fast Fourier transform pattern (FFT) in Figure 3f,h indicate the $\{112\}$ planes where the lattice spacing is 3.5 Å and the $\{200\}$ planes where the lattice spacing is 4.4 Å for CoMoO_4 observed along the $[021]$ axis, as can be indexed from the combination of Figure 3g and its simulated corresponding FFT (Figure 3i).

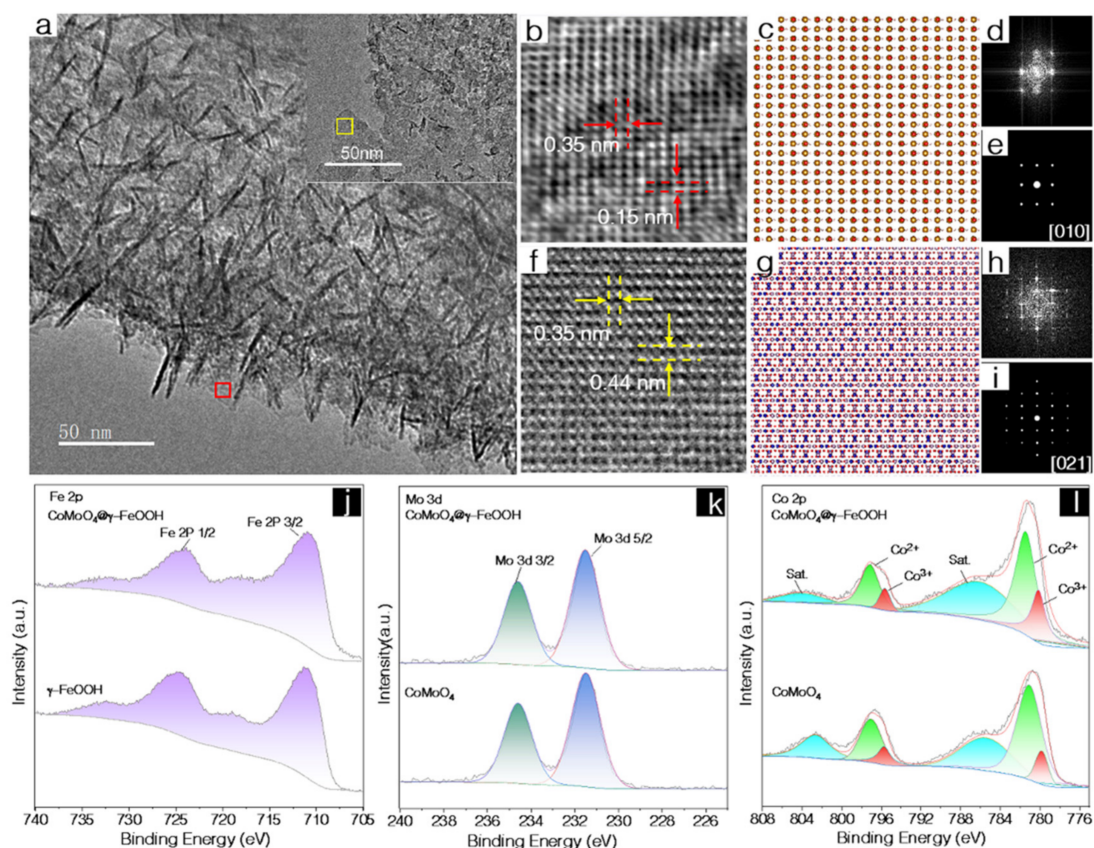


Figure 3. (a) Low magnification TEM image of $\text{CoMoO}_4@ \gamma\text{-FeOOH}$'s heterostructure, insets show the $\gamma\text{-FeOOH}$ region (red rectangle), and CoMoO_4 region (yellow rectangle). (b) Magnified HRTEM view of the crystalline region of $\gamma\text{-FeOOH}$. (c) The crystal structure model of $\gamma\text{-FeOOH}$ observed along the [010] axis. (d) FFT of the (b,e) simulated FFT of the crystal structure model of $\gamma\text{-FeOOH}$ observed along the [010] axis. (e) Simulated FFT of the crystal structure model of $\gamma\text{-FeOOH}$ observed along the [010] axis. (f) Magnified HRTEM view of the crystalline region of CoMoO_4 . (g) The crystal structure model of CoMoO_4 observed along the [021] axis. (h) FFT of the (f,i) simulated FFT of the crystal structure. (i) Simulated FFT of the crystal structure. (j) High-resolution Fe 2p XPS spectra of $\text{CoMoO}_4@ \gamma\text{-FeOOH}$ and CoMoO_4 . (k) High-resolution Mo 3d XPS spectra of $\text{CoMoO}_4@ \gamma\text{-FeOOH}$ and CoMoO_4 . (l) High-resolution Co 2p XPS spectra of $\text{CoMoO}_4@ \gamma\text{-FeOOH}$ and $\gamma\text{-FeOOH}$.

Previous reports have demonstrated that the electronic structure of an active site is highly related to the catalytic activity and could be adequately modulated by constructing heterostructures [30,31]. Hence, X-ray photoelectron spectroscopy (XPS) was employed to study detailed atomic and electronic structural information. As shown in Figure S5a, the survey spectrum of $\text{CoMoO}_4@ \gamma\text{-FeOOH}$ shows the coexistence of Co, Fe, Mo, O, and C, indicating the successful growth of $\gamma\text{-FeOOH}$ on the CoMoO_4 nanosheets. In the high-resolution XPS spectra of Fe 2p ($\gamma\text{-FeOOH}$ and $\text{CoMoO}_4@ \gamma\text{-FeOOH}$), the two peaks located at about 711.2 and 724.7 eV can be attributed to the Fe^{2+} 2p 3/2 and Fe^{2+} 2p 1/2 of Fe-O species [32], respectively (Figure 3j). In addition, similar XPS fine spectra of Mo in the CoMoO_4 and $\text{CoMoO}_4@ \gamma\text{-FeOOH}$ collectively suggests the similar coordination environments of Fe ions and Mo ions in the $\text{CoMoO}_4@ \gamma\text{-FeOOH}$ and the corresponding single components (Figure 3k). The peaks at about 780.7 eV (2p 3/2) and 796.8 eV (2p 1/2) in the spectra of Co are consistent with the Co-O species [33] (Figure 3l). However, the fitted results indicate that the peak ratio of $\text{Co}^{2+}/\text{Co}^{3+}$ decreases after decorating $\gamma\text{-FeOOH}$ on the surface of the CoMoO_4 nanosheets, indicating that the ion exchange of the Co and Fe ions in the $\gamma\text{-FeOOH}$ resulted in the formation of Co-doped $\gamma\text{-FeOOH}$ with partial Co atoms possessing a higher valence. It has been widely reported that active sites with a higher valence could enhance the chemisorption of OH^- , complement the formation of

MOOH (M represents metal, such as Co or Ni) through nucleophilic attack during OER, and are generally regarded as the active sites for OER [34]. Therefore, the as-synthesized biphasic $\text{CoMoO}_4@ \gamma\text{-FeOOH}$ nanosheets offer a great opportunity to evoke synergistic electrocatalysis towards OER.

The electrochemical behaviors of the as-prepared and commercial catalysts were evaluated with a three-electrode system in O_2 -saturated 1 M KOH electrolytes. To evaluate the OER activity of these materials, RuO_2 was deposited on the Ni foam as a reference with the same loading. The linear sweep voltammetry (LSV) curves (Figure 4a) with *iR*-compensation show that the $\text{CoMoO}_4@ \gamma\text{-FeOOH}$ catalyst exhibits the most optimal performance, with an outstanding OER current density of 10 mA cm^{-2} with a low overpotential of 243.1 mV, which is 34.1, 75.3, 48.9, and 146.9 mV lower than that of $\gamma\text{-FeOOH}$, CoMoO_4 , RuO_2 , and Ni foam (Figure 4a,b). Furthermore, very small overpotentials of 270.3 and 278.5 mV are enough to reach a high current density of 50 mA cm^{-2} and 100 mA cm^{-2} for the $\text{CoMoO}_4@ \gamma\text{-FeOOH}$ electrode, which is highly competitive when compared to other previously reported OER electrocatalysts (Supplementary Table S1) [35–47]. Figure 4c shows the Tafel plots of the sample catalysts, where the $\text{CoMoO}_4@ \gamma\text{-FeOOH}$ presented the lowest Tafel slope of $46.58 \text{ mV dec}^{-1}$ in contrast to those of $\gamma\text{-FeOOH}$ ($60.71 \text{ mV dec}^{-1}$), RuO_2 ($51.20 \text{ mV dec}^{-1}$), and CoMoO_4 ($83.85 \text{ mV dec}^{-1}$), indicating the rapid kinetics of $\text{CoMoO}_4@ \gamma\text{-FeOOH}$. The electrochemically active surface area (ECSA) was evaluated by the electrochemical double-layer capacitance (C_{dl}) (Figure S6). As seen in Figure 4d, the CoMoO_4 exhibits a larger double-layer capacitance (C_{dl}) value (3.52 mF cm^{-2}) than those of $\text{CoMoO}_4@ \gamma\text{-FeOOH}$ (1.75 mF cm^{-2}) and $\gamma\text{-FeOOH}$ (0.62 mF cm^{-2}), indicating that CoMoO_4 could complement the exposure of the active site and largely enhance the ECSA of $\text{CoMoO}_4@ \gamma\text{-FeOOH}$. Comparing the results, the $\gamma\text{-FeOOH}$ exhibits a much higher activity relative to CoMoO_4 towards OER, suggesting that the Co and Fe sites in the Co-doped $\gamma\text{-FeOOH}$ are both performing as real OER active sites, and that the presence of CoMoO_4 modifies the environmental conditions of the active sites. Therefore, the core-shell structure of $\text{CoMoO}_4@ \gamma\text{-FeOOH}$ not only improves the ECSA of active components by moderating the dispersion of $\gamma\text{-FeOOH}$, but also enhances the intrinsic activity of $\gamma\text{-FeOOH}$ through the doping of Co atoms, which collectively leads to the higher electronic activity and lower overpotential of $\text{CoMoO}_4@ \gamma\text{-FeOOH}$ compared to the single components. The stability was also evaluated via chronopotentiometry experiments without *iR* compensation for three constant cycles that comprised a test duration of 36 h at multcurrent densities (Figure 4e). The overpotential remained stable for all the cycles; about 283.1, 325.7, and 355.0 mV were required to reach the current densities of 10, 50, and 100 mA cm^{-2} , respectively, indicating that the $\text{CoMoO}_4@ \gamma\text{-FeOOH}$ heterostructure possesses a superb durability. Faradaic efficiency measurements were also tested to assess the difference between the actual efficiency and the theoretical efficiency of the $\text{CoMoO}_4@ \gamma\text{-FeOOH}$ electrode (Figure S7). The detailed test and the calculated method could be referenced with the reported literature [48]. The results exhibited a Faradaic efficiency of about 93.9% after applying a current density of 10 mA cm^{-2} for 5 h, suggesting that all the applied electrons were almost completely used for water oxidation under the consideration of an experimental error.

It has been widely demonstrated that most of the transition metal-based electrocatalysts will undergo a structural transformation during the OER process. Therefore, detailed structure tests were carried out for the catalysts after the LSV test to explore the intrinsic origins of the high OER activity. As shown in Figures S8 and S9, the morphology of CoMoO_4 and $\gamma\text{-FeOOH}$ showed limited changes after the LSV test, while the morphology of $\text{CoMoO}_4@ \gamma\text{-FeOOH}$ exhibited obvious changes, and the $\gamma\text{-FeOOH}$ nanosheets on the CoMoO_4 turned into some nanoparticles that closely embedded into the surface of CoMoO_4 . The Raman and selected area electron diffraction (SAED) methods were used to investigate the structural evolution of $\text{CoMoO}_4@ \gamma\text{-FeOOH}$ after the LSV test. As shown in Figure S10, the $\text{CoMoO}_4@ \gamma\text{-FeOOH}$ after the LSV test showed typical peaks for Fe-O, Co-O-Mo, and Mo-O vibrations that were similar to the initial Raman spectrum of $\text{CoMoO}_4@ \gamma\text{-FeOOH}$. The HAADF STEM mapping (Figure 5a) results revealed that the $\text{CoMoO}_4@ \gamma\text{-FeOOH}$

after the LSV test retained its initial element composition and exhibited a homogeneous dispersion of the Mo, Co, and Fe atoms. Detailed phase information was collected through SAED. The SAED pattern (Figure 5b) exhibits a typical diffraction pattern characteristic of polycrystalline materials, of which the diffraction pattern and the radially-averaged diffraction rings (Figure 5c) can be adequately indexed to both the CoMoO_4 (marked with yellow wires) and $\gamma\text{-FeOOH}$ phases (marked with red wires) of the heterostructure. The XPS spectra of $\text{CoMoO}_4@ \gamma\text{-FeOOH}$ after the LSV test showed a similar elemental composition and valence (Figure S11). These limited changes in the chemical environment and phase composition indicate that the $\text{CoMoO}_4@ \gamma\text{-FeOOH}$ adequately preserved its initial structure under OER conditions, which may largely contribute to its superb stability in OER reactions.

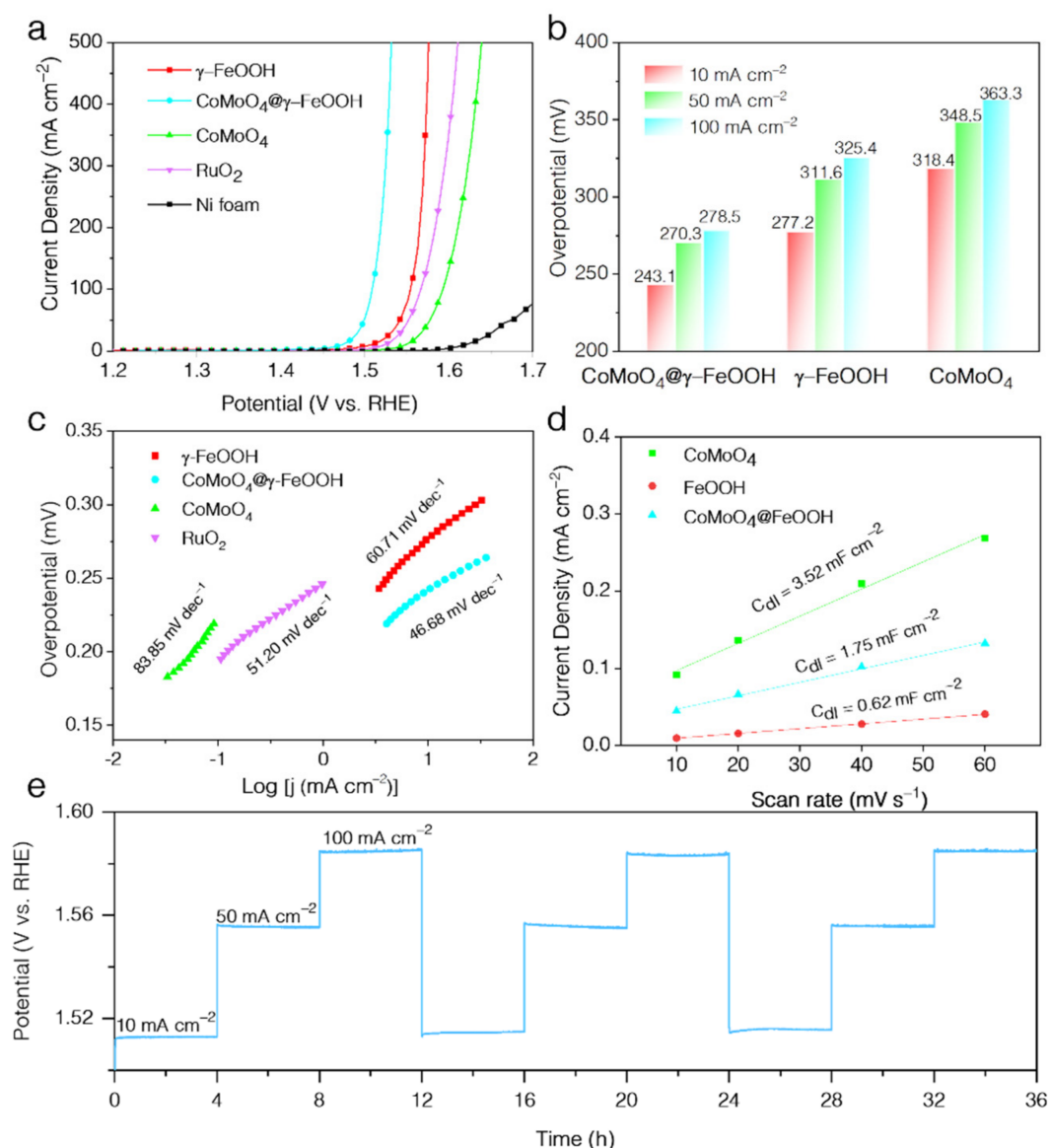


Figure 4. (a) LSV curves of CoMoO_4 , $\text{CoMoO}_4@ \gamma\text{-FeOOH}$, $\gamma\text{-FeOOH}$, RuO_2 , and Ni foam in 1.0 M KOH. (b) Comparison of the overpotentials at 10 mA cm^{-2} , 50 mA cm^{-2} , and 100 mA cm^{-2} for CoMoO_4 , $\text{CoMoO}_4@ \gamma\text{-FeOOH}$, and $\gamma\text{-FeOOH}$. (c) Tafel plots of CoMoO_4 , $\text{CoMoO}_4@ \gamma\text{-FeOOH}$, $\gamma\text{-FeOOH}$, and RuO_2 . (d) CV current density versus scan rate of CoMoO_4 , $\text{CoMoO}_4@ \gamma\text{-FeOOH}$, and $\gamma\text{-FeOOH}$. (e) Durability test of $\text{CoMoO}_4@ \gamma\text{-FeOOH}$ in 1.0 M KOH at constant 10 mA cm^{-2} , 50 mA cm^{-2} , and 100 mA cm^{-2} .

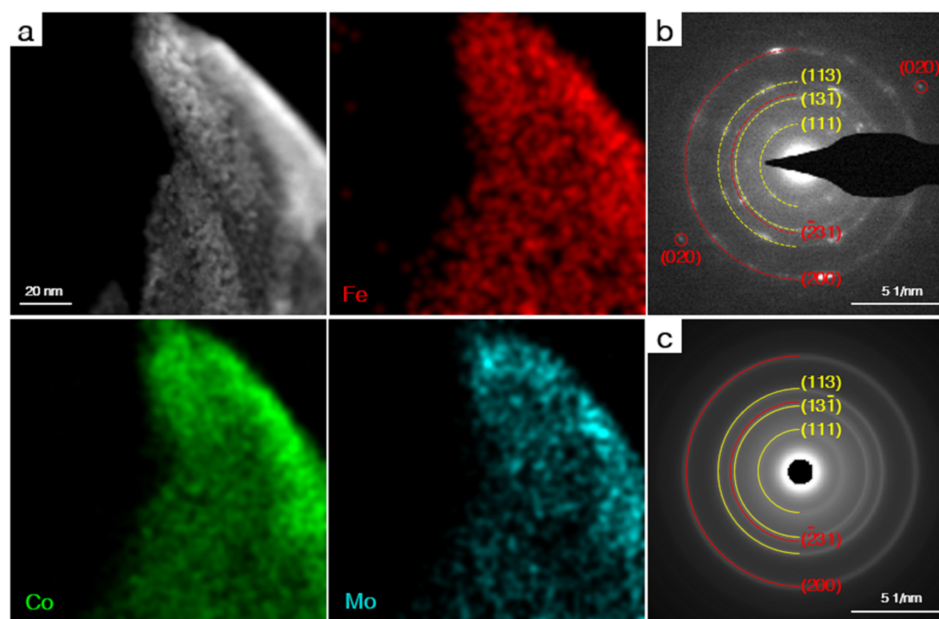


Figure 5. (a) HAADF STEM and corresponding EDS mapping images of $\text{CoMoO}_4@ \gamma\text{-FeOOH}$ after LSV test. (b) SAED and (c) Radially-averaged patterns of $\text{CoMoO}_4@ \gamma\text{-FeOOH}$ after LSV test.

4. Conclusions

In conclusion, we have demonstrated a general strategy for constructing highly efficient OER catalysts through the post-synthesis of multi-metal oxyhydroxides on stable support frameworks. An HRTEM was employed to successfully confirm the synthesis of a sheet-like $\text{CoMoO}_4@ \gamma\text{-FeOOH}$ core-shell structure, and EDS mapping proved that the Co atoms immersed into the $\gamma\text{-FeOOH}$ to form dual-metal entities. The as-prepared catalysts show a distinguished OER performance with a low overpotential of 243.1 mV under a current density of 10 mA cm^{-2} . Moreover, the $\text{CoMoO}_4@ \gamma\text{-FeOOH}$ presented a very low Tafel slope of $46.58 \text{ mV dec}^{-1}$, as well as a very highly electrochemically active surface area. We further investigated the catalyst structure and composition after 36 h of electrolysis, which demonstrated a very high stability in accordance with our design purpose.

Supplementary Materials: The following supporting information can be downloaded at: <https://www.mdpi.com/article/10.3390/nano12132215/s1>, Figure S1: (a) HAADF STEM and EDS mapping images of $\text{CoMoO}_4@ \gamma\text{-FeOOH}$. (b) EDS Line scan spectrum of the area marked with blue arrow in (a). Figure S2: (a) Low- and (b,c) high-magnification SEM images of $\gamma\text{-FeOOH}$, (d) TEM image of $\gamma\text{-FeOOH}$ powder synthesized without Ni foam substrate. Figure S3: (a) XRD patterns of CoMoO_4 and $\text{CoMoO}_4@ \gamma\text{-FeOOH}$, (b) XRD pattern of $\gamma\text{-FeOOH}$. Figure S4: Raman spectra of CoMoO_4 , $\text{CoMoO}_4@ \gamma\text{-FeOOH}$, and $\gamma\text{-FeOOH}$. Figure S5: XPS survey spectra of (a) $\text{CoMoO}_4@ \gamma\text{-FeOOH}$, (b) CoMoO_4 , and (c) $\gamma\text{-FeOOH}$. Figure S6: CV curves of (a) CoMoO_4 , (b) $\text{CoMoO}_4@ \gamma\text{-FeOOH}$, and (c) $\gamma\text{-FeOOH}$ acquired at various scan rates. Figure S7: Faradaic efficiency of $\text{CoMoO}_4@ \gamma\text{-FeOOH}$ for the theoretically calculated and experimentally measured O_2 at a current density of 10 mA cm^{-2} . Figure S8: SEM images of catalysts after LSV test, (a–c) CoMoO_4 , (d–f) $\gamma\text{-FeOOH}$. Figure S9: (a–c) SEM images of $\text{CoMoO}_4@ \gamma\text{-FeOOH}$ after LSV test with different magnifications. Figure S10: Raman spectra of $\text{CoMoO}_4@ \gamma\text{-FeOOH}$ after LSV test. Figure S11: (a) XPS survey spectrum, (b) high-resolution Co 2p XPS spectrum, (c) high-resolution Mo 3d XPS spectrum, (d) high-resolution Fe 2p XPS spectrum of $\text{CoMoO}_4@ \gamma\text{-FeOOH}$ after LSV test. Table S1: Comparison of OER performances between $\text{CoMoO}_4@ \gamma\text{-FeOOH}$ electrode and recently reported electrocatalysts in alkaline solution. References [35–47] have been cited in the Supplementary Materials.

Author Contributions: Conceptualization, H.S., J.L. (Jingjing Li) and G.S.; methodology, G.S. and A.A.M.; software, A.A.M.; validation, Y.Z., Z.Z. and J.L. (Juan Luo); formal analysis, Y.Z.; investigation, Z.Z.; resources, J.L. (Juan Luo); data curation, H.S. and J.L. (Jingjing Li); writing—original draft preparation, H.S., J.L. (Jingjing Li) and G.S.; writing—review and editing, W.S.; visualization, Z.Z.; supervision, W.S.; project administration, W.S.; funding acquisition, W.S. All authors have read and agreed to the published version of the manuscript.

Funding: This work is supported by the National Natural Science Foundation of China (22075249, 51802281), and the Zhejiang Provincial Natural Science Foundation (LY21B010006).

Data Availability Statement: The data that support the findings of this study are available from the corresponding authors upon reasonable request.

Conflicts of Interest: There are no conflict of interest to declare.

References

1. Liu, P.; Liu, W.; Huang, Y.; Li, P.; Yan, J.; Liu, K. Mesoporous Hollow Carbon Spheres Boosted, Integrated High Performance Aqueous Zn-Ion Energy Storage. *Energy Storage Mater.* **2020**, *25*, 858–865. [[CrossRef](#)]
2. Liu, P.; Zhang, Z.; Hao, R.; Huang, Y.; Liu, W.; Tan, Y.; Li, P.; Yan, J.; Liu, K. Ultra-Highly Stable Zinc Metal Anode via 3D-Printed g-C₃N₄ Modulating Interface for Long Life Energy Storage Systems. *Chem. Eng. J.* **2021**, *403*, 126425. [[CrossRef](#)]
3. Sui, X.; Zhang, L.; Li, J.; Doyle-Davis, K.; Li, R.; Wang, Z.; Sun, X. Enhancing Metal–Support Interaction by in Situ Ion-Exchanging Strategy for High Performance Pt Catalysts in Hydrogen Evolution Reaction. *J. Mater. Chem. A* **2020**, *8*, 16582–16589. [[CrossRef](#)]
4. Sui, X.; Zhang, L.; Li, J.; Doyle-Davis, K.; Li, R.; Wang, Z.; Sun, X. Advanced Support Materials and Interactions for Atomically Dispersed Noble-Metal Catalysts: From Support Effects to Design Strategies. *Adv. Energy Mater.* **2022**, *12*, 2102556. [[CrossRef](#)]
5. Guan, J.; Shao, L.; Yu, L.; Wang, S.; Shi, X.; Cai, J.; Sun, Z. Two-Dimensional Mg_{0.2}V₂O₅·nH₂O Nanobelts Derived from V₄C₃ MXenes for Highly Stable Aqueous Zinc Ion Batteries. *Chem. Eng. J.* **2022**, *443*, 136502. [[CrossRef](#)]
6. Yuk, S.F.; Cooper, V.R. Tuning Oxygen Electrocatalysis via Strain on LaNiO₃(001). *Phys. Chem. Chem. Phys.* **2019**, *21*, 4738–4745. [[CrossRef](#)]
7. Zhang, X.; Zhang, W.; Dai, J.; Sun, M.; Zhao, J.; Ji, L.; Chen, L.; Zeng, F.; Yang, F.; Huang, B.; et al. Carboxylated Carbon Nanotubes with High Electrocatalytic Activity for Oxygen Evolution in Acidic Conditions. *InfoMat* **2022**, *4*, e12273. [[CrossRef](#)]
8. Jin, H.; Guo, C.; Liu, X.; Liu, J.; Vasileff, A.; Jiao, Y.; Zheng, Y.; Qiao, S.-Z. Emerging Two-Dimensional Nanomaterials for Electrocatalysis. *Chem. Rev.* **2018**, *118*, 6337–6408. [[CrossRef](#)]
9. Zhang, Z.; Wang, C.; Ma, X.; Liu, F.; Xiao, H.; Zhang, J.; Lin, Z.; Hao, Z. Engineering Ultrafine NiFe-LDH into Self-Supporting Nanosheets: Separation-and-Reunion Strategy to Expose Additional Edge Sites for Oxygen Evolution. *Small* **2021**, *17*, 2103785. [[CrossRef](#)]
10. Saylor, R.I.; Hunter, B.M.; Fu, W.; Gray, H.B.; Britt, R.D. EPR Spectroscopy of Iron- and Nickel-Doped [ZnAl]-Layered Double Hydroxides: Modeling Active Sites in Heterogeneous Water Oxidation Catalysts. *J. Am. Chem. Soc.* **2020**, *142*, 1838–1845. [[CrossRef](#)]
11. Haber, J.A.; Anzenburg, E.; Yano, J.; Kisielowski, C.; Gregoire, J.M. Multiphase Nanostructure of a Quinary Metal Oxide Electrocatalyst Reveals a New Direction for OER Electrocatalyst Design. *Adv. Energy Mater.* **2015**, *5*, 1402307. [[CrossRef](#)]
12. Li, L.; Gao, W.; Tang, K.; Lei, M.; Yao, B.; Qi, W.; Wen, D. Structure Engineering of Ni₂P by Mo Doping for Robust Electrocatalytic Water and Methanol Oxidation Reactions. *Electrochimica Acta* **2021**, *369*, 137692. [[CrossRef](#)]
13. Zhou, J.; Yuan, L.; Wang, J.; Song, L.; You, Y.; Zhou, R.; Zhang, J.; Xu, J. Combinational Modulations of NiSe₂ Nanodendrites by Phase Engineering and Iron-Doping towards an Efficient Oxygen Evolution Reaction. *J. Mater. Chem. A* **2020**, *8*, 8113–8120. [[CrossRef](#)]
14. Liu, H.; He, Q.; Jiang, H.; Lin, Y.; Zhang, Y.; Habib, M.; Chen, S.; Song, L. Electronic Structure Reconfiguration toward Pyrite NiS₂ via Engineered Heteroatom Defect Boosting Overall Water Splitting. *ACS Nano* **2017**, *11*, 11574–11583. [[CrossRef](#)] [[PubMed](#)]
15. Yuan, Y.; Adimi, S.; Guo, X.; Thomas, T.; Zhu, Y.; Guo, H.; Priyanga, G.S.; Yoo, P.; Wang, J.; Chen, J.; et al. A Surface-Oxide-Rich Activation Layer (SOAL) on Ni₂Mo₃N for a Rapid and Durable Oxygen Evolution Reaction. *Angew. Chem. Int. Ed.* **2020**, *59*, 18036–18041. [[CrossRef](#)]
16. Liu, X.; Meng, J.; Zhu, J.; Huang, M.; Wen, B.; Guo, R.; Mai, L. Comprehensive Understandings into Complete Reconstruction of Precatalysts: Synthesis, Applications, and Characterizations. *Adv. Mater.* **2021**, *33*, 2007344. [[CrossRef](#)]
17. Wang, Y.; Zhu, Y.; Zhao, S.; She, S.; Zhang, F.; Chen, Y.; Williams, T.; Gengenbach, T.; Zu, L.; Mao, H.; et al. Anion Etching for Accessing Rapid and Deep Self-Reconstruction of Precatalysts for Water Oxidation. *Matter* **2020**, *3*, 2124–2137. [[CrossRef](#)]
18. Wang, K.; Du, H.; He, S.; Liu, L.; Yang, K.; Sun, J.; Liu, Y.; Du, Z.; Xie, L.; Ai, W.; et al. Kinetically Controlled, Scalable Synthesis of γ-FeOOH Nanosheet Arrays on Nickel Foam toward Efficient Oxygen Evolution: The Key Role of In-Situ-Generated γ-NiOOH. *Adv. Mater.* **2021**, *33*, 2005587. [[CrossRef](#)]
19. Zhou, X.; Zi, Y.; Xu, L.; Li, T.; Yang, J.; Tang, J. Core–Shell-Structured Prussian Blue Analogues Ternary Metal Phosphides as Efficient Bifunctional Electrocatalysts for OER and HER. *Inorg. Chem.* **2021**, *60*, 11661–11671. [[CrossRef](#)]

20. Lv, Y.; Duan, S.; Zhu, Y.; Yin, P.; Wang, R. Enhanced OER Performances of Au@NiCo₂S₄ Core-Shell Heterostructure. *Nanomaterials* **2020**, *10*, 611. [[CrossRef](#)]
21. Liu, Y.; Li, Y.; Wu, Q.; Su, Z.; Wang, B.; Chen, Y.; Wang, S. Hollow CoP/FeP₄ Heterostructural Nanorods Interwoven by CNT as a Highly Efficient Electrocatalyst for Oxygen Evolution Reactions. *Nanomaterials* **2021**, *11*, 1450. [[CrossRef](#)] [[PubMed](#)]
22. Rehman, K.U.; Airam, S.; Lin, X.; Gao, J.; Guo, Q.; Zhang, Z. In Situ Formation of Surface-Induced Oxygen Vacancies in Co₉S₈/CoO/NC as a Bifunctional Electrocatalyst for Improved Oxygen and Hydrogen Evolution Reactions. *Nanomaterials* **2021**, *11*, 2237. [[CrossRef](#)] [[PubMed](#)]
23. Jeon, J.; Park, K.R.; Kim, K.M.; Ko, D.; Han, H.; Oh, N.; Yeo, S.; Ahn, C.; Mhin, S. CoFeS₂@CoS₂ Nanocubes Entangled with CNT for Efficient Bifunctional Performance for Oxygen Evolution and Oxygen Reduction Reactions. *Nanomaterials* **2022**, *12*, 983. [[CrossRef](#)] [[PubMed](#)]
24. Hu, Z.; Xu, Y.; Xiang, W.; Guo, X.; Tong, Y.; Xu, J.; Yang, C. Amorphous Ni-P-S@FeOOH/CC Catalyst for High Oxygen Evolution Activity: Preparation, Characterization and Modeling. *Chem. Eng. Sci.* **2022**, *258*, 117761. [[CrossRef](#)]
25. Tian, X.; Yi, P.; Sun, J.; Li, C.; Liu, R.; Sun, J.-K. The Scalable Solid-State Synthesis of a Ni₅P₄/Ni₂P-FeNi Alloy Encapsulated into a Hierarchical Porous Carbon Framework for Efficient Oxygen Evolution Reactions. *Nanomaterials* **2022**, *12*, 1848. [[CrossRef](#)]
26. Yu, X.; Chen, W.; Cai, J.; Lu, X.; Sun, Z. Oxygen Vacancy-Rich MnO Nanoflakes/N-Doped Carbon Nanotubes Modified Separator Enabling Chemisorption and Catalytic Conversion of Polysulfides for Li-S Batteries. *J. Colloid Interface Sci.* **2022**, *610*, 407–417. [[CrossRef](#)]
27. Barmi, M.J.; Minakshi, M. Tuning the Redox Properties of the Nanostructured CoMoO₄ Electrode: Effects of Surfactant Content and Synthesis Temperature. *ChemPlusChem* **2016**, *81*, 964–977. [[CrossRef](#)]
28. Minakshi, M. Lithium Intercalation into Amorphous FePO₄ Cathode in Aqueous Solutions. *Electrochimica Acta* **2010**, *55*, 9174–9178. [[CrossRef](#)]
29. Xie, W.; Huang, J.; Huang, L.; Geng, S.; Song, S.; Tsiakaras, P.; Wang, Y. Novel Fluorine-Doped Cobalt Molybdate Nanosheets with Enriched Oxygen-Vacancies for Improved Oxygen Evolution Reaction Activity. *Appl. Catal. B Environ.* **2022**, *303*, 120871. [[CrossRef](#)]
30. Wu, T.; Song, E.; Zhang, S.; Luo, M.; Zhao, C.; Zhao, W.; Liu, J.; Huang, F. Engineering Metallic Heterostructure Based on Ni₃N and 2M-MoS₂ for Alkaline Water Electrolysis with Industry-Compatible Current Density and Stability. *Adv. Mater.* **2022**, *34*, 2108505. [[CrossRef](#)]
31. Li, T.; Yin, J.; Sun, D.; Zhang, M.; Pang, H.; Xu, L.; Zhang, Y.; Yang, J.; Tang, Y.; Xue, J. Manipulation of Mott–Schottky Ni/CeO₂ Heterojunctions into N-Doped Carbon Nanofibers for High-Efficiency Electrochemical Water Splitting. *Small* **2022**, *18*, 2106592. [[CrossRef](#)] [[PubMed](#)]
32. Li, L.; Bi, H.; Gai, S.; He, F.; Gao, P.; Dai, Y.; Zhang, X.; Yang, D.; Zhang, M.; Yang, P. Uniformly Dispersed ZnFe₂O₄ Nanoparticles on Nitrogen-Modified Graphene for High-Performance Supercapacitor as Electrode. *Sci. Rep.* **2017**, *7*, 43116. [[CrossRef](#)] [[PubMed](#)]
33. Gong, C.; Li, W.; Lei, Y.; He, X.; Chen, H.; Du, X.; Fang, W.; Wang, D.; Zhao, L. Interfacial Engineering of ZIF-67 Derived CoSe/Co(OH)₂ Catalysts for Efficient Overall Water Splitting. *Compos. Part B Eng.* **2022**, *236*, 109823. [[CrossRef](#)]
34. Wan, K.; Luo, J.; Zhou, C.; Zhang, T.; Arbiol, J.; Lu, X.; Mao, B.-W.; Zhang, X.; Franssaer, J. Hierarchical Porous Ni₃S₄ with Enriched High-Valence Ni Sites as a Robust Electrocatalyst for Efficient Oxygen Evolution Reaction. *Adv. Funct. Mater.* **2019**, *29*, 1900315. [[CrossRef](#)]
35. Choi, J.; Kim, D.; Zheng, W.; Yan, B.; Li, Y.; Lee, L.Y.S.; Piao, Y. Interface Engineered NiFe₂O_{4-x}/NiMoO₄ Nanowire Arrays for Electrochemical Oxygen Evolution. *Appl. Catal. B Environ.* **2021**, *286*, 119857. [[CrossRef](#)]
36. Zheng, M.; Guo, K.; Jiang, W.-J.; Tang, T.; Wang, X.; Zhou, P.; Du, J.; Zhao, Y.; Xu, C.; Hu, J.-S. When MoS₂ Meets FeOOH: A “One-Stone-Two-Birds” Heterostructure as a Bifunctional Electrocatalyst for Efficient Alkaline Water Splitting. *Appl. Catal. B Environ.* **2019**, *244*, 1004–1012. [[CrossRef](#)]
37. Liu, P.F.; Yang, S.; Zhang, B.; Yang, H.G. Defect-Rich Ultrathin Cobalt–Iron Layered Double Hydroxide for Electrochemical Overall Water Splitting. *ACS Appl. Mater. Interfaces* **2016**, *8*, 34474–34481. [[CrossRef](#)]
38. Qiu, Z.; Ma, Y.; Edvinsson, T. In Operando Raman Investigation of Fe Doping Influence on Catalytic NiO Intermediates for Enhanced Overall Water Splitting. *Nano Energy* **2019**, *66*, 104118. [[CrossRef](#)]
39. Xiong, Y.; Xu, L.; Jin, C.; Sun, Q. Interface-Engineered Atomically Thin Ni₃S₂/MnO₂ Heterogeneous Nanoarrays for Efficient Overall Water Splitting in Alkaline Media. *Appl. Catal. B Environ.* **2019**, *254*, 329–338. [[CrossRef](#)]
40. Che, Q.; Li, Q.; Chen, X.; Tan, Y.; Xu, X. Assembling Amorphous (Fe-Ni)Co_x-OH/Ni₃S₂ Nanohybrids with S-Vacancy and Interfacial Effects as an Ultra-Highly Efficient Electrocatalyst: Inner Investigation of Mechanism for Alkaline Water-to-Hydrogen/Oxygen Conversion. *Appl. Catal. B Environ.* **2020**, *263*, 118338. [[CrossRef](#)]
41. Li, Z.; Niu, W.; Zhou, L.; Yang, Y. Phosphorus and Aluminum Codoped Porous NiO Nanosheets as Highly Efficient Electrocatalysts for Overall Water Splitting. *ACS Energy Lett.* **2018**, *3*, 892–898. [[CrossRef](#)]
42. Jin, Y.; Huang, S.; Yue, X.; Shu, C.; Shen, P.K. Highly Stable and Efficient Non-Precious Metal Electrocatalysts of Mo-Doped NiOOH Nanosheets for Oxygen Evolution Reaction. *Int. J. Hydrog. Energy* **2018**, *43*, 12140–12145. [[CrossRef](#)]
43. Hao, S.; Chen, L.; Yu, C.; Yang, B.; Li, Z.; Hou, Y.; Lei, L.; Zhang, X. NiCoMo Hydroxide Nanosheet Arrays Synthesized via Chloride Corrosion for Overall Water Splitting. *ACS Energy Lett.* **2019**, *4*, 952–959. [[CrossRef](#)]
44. Guan, C.; Xiao, W.; Wu, H.; Liu, X.; Zang, W.; Zhang, H.; Ding, J.; Feng, Y.P.; Pennycook, S.J.; Wang, J. Hollow Mo-Doped CoP Nanoarrays for Efficient Overall Water Splitting. *Nano Energy* **2018**, *48*, 73–80. [[CrossRef](#)]

45. Wang, D.; Li, Q.; Han, C.; Xing, Z.; Yang, X. When NiO@Ni Meets WS₂ Nanosheet Array: A Highly Efficient and Ultrastable Electrocatalyst for Overall Water Splitting. *ACS Cent. Sci.* **2018**, *4*, 112–119. [[CrossRef](#)]
46. Luo, X.; Shao, Q.; Pi, Y.; Huang, X. Trimetallic Molybdate Nanobelts as Active and Stable Electrocatalysts for the Oxygen Evolution Reaction. *ACS Catal.* **2019**, *9*, 1013–1018. [[CrossRef](#)]
47. Xu, H.; Shang, H.; Wang, C.; Jin, L.; Chen, C.; Wang, C.; Du, Y. Three-Dimensional Open CoMoO_x/CoMoS_x/CoS_x Nanobox Electrocatalysts for Efficient Oxygen Evolution Reaction. *Appl. Catal. B Environ.* **2020**, *265*, 118605. [[CrossRef](#)]
48. Park, H.; Park, B.H.; Choi, J.; Kim, S.; Kim, T.; Youn, Y.-S.; Son, N.; Kim, J.H.; Kang, M. Enhanced Electrochemical Properties and OER Performances by Cu Substitution in NiCo₂O₄ Spinel Structure. *Nanomaterials* **2020**, *10*, 1727. [[CrossRef](#)]